

# Non-Gaussian Photon Correlations in Weakly Coupled Atomic Ensembles

YangMing Wang<sup>1,2,\*</sup> and Sahand Mahmoodian<sup>1,3,†</sup>

<sup>1</sup>*ARC Centre of Excellence for Engineered Quantum Systems,  
School of Physics, The University of Sydney, Sydney, NSW 2006, Australia*

<sup>2</sup>*Sydney Quantum Academy, Sydney, NSW, Australia*

<sup>3</sup>*Institute for Photonics and Optical Sciences (IPOS),  
School of Physics, The University of Sydney, NSW 2006, Australia*

(Dated: September 5, 2025)

We develop a scattering theory formalism and use it to predict that a resonantly driven atomic ensemble weakly coupled to an optical mode can generate light with non-Gaussian correlations. Our approach—based on a perturbative diagrammatic expansion of multi-photon interactions—shows that photon-photon interaction mediated by the emitters causes the transmitted light to have a non-vanishing connected third-order correlation function  $g_c^{(3)}$ . We explain the temporal pattern of  $g_c^{(3)}$  using the interaction processes in our diagrammatic expansion. A quantitative comparison with cascaded master equation simulations for small ensembles with optical depth  $OD \leq 2$  confirms that the perturbative results remain accurate across experimentally relevant optical depths and for drive strengths large enough to make the predicted non-Gaussian signatures detectable. We anticipate that state-of-the-art nanofibre-coupled atomic ensembles can experimentally demonstrate our predictions.

**Introduction.**—Photon-photon interactions in optically driven atomic ensembles can alter the quantum state of an incident laser field. Here, the interplay of nonlinear interactions, due to the two-level atoms in the ensemble, and the elastic scattering of laser light out of the ensemble allows manipulating the quantum nature of light [1, 2]. For example, photons can become strongly correlated, modifying both intensity correlations [3–5] and electric field fluctuations [6, 7]. Such works have largely focused on quantifying two-body photon correlations. On the other hand, three-photon correlations, including non-Gaussian correlations, have been measured in other quantum optics systems [8–12], and very recently an atomic ensemble was also used to demonstrate the generation of non-Gaussian light by observing violations of the Siegert relation [13]. Here, non-Gaussian refers to light whose observables or correlators cannot be described by the mean-values and covariance of its electric field quadratures [14].

Despite experimental advances, a tractable theoretical framework for describing three-photon dynamics or the presence of non-Gaussian correlations in large atomic ensembles remains elusive. Dilute ensembles are often modeled using the Maxwell-Bloch equations [15–18], which, under a mean-field approximation, provide a minimal semiclassical description incorporating unidirectional coupling to a one-dimensional continuum of photon modes. To capture quantum correlations beyond the mean-field level, one can employ a complete cascaded master equation [19, 20]. However, for large ensembles, the exponential growth of the Hilbert space with system size renders the direct computation of higher-order correlation functions, such as  $g^{(3)}$ , challenging, even if employing cumulant expansion [21, 22] or matrix-product operator [23, 24] methods.

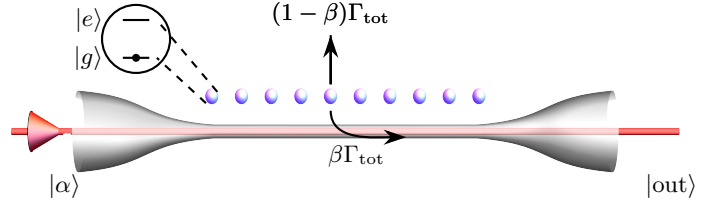


FIG. 1. An array of  $M$  chirally coupled two-level atoms (depicted as blue balls) resonantly driven by an external coherent field  $|\alpha\rangle$  producing a strongly correlated output photon state  $|\text{out}\rangle$ . Each atom couples to the waveguide with a decay rate  $\beta\Gamma_{\text{tot}}$  and to external loss channel with a decay rate  $(1 - \beta)\Gamma_{\text{tot}}$ .

In this work, we propose an analytic and diagrammatic framework to calculate up to three-photon transport through the atomic ensemble. Using the Maxwell-Bloch approach, the ensemble can be considered to be an array of atoms unidirectionally coupled to an optical nanofibre as shown in Fig. 1. The coupling efficiency between each atom and waveguide is weak  $\beta \ll 1$  while the number of atoms  $M \gg 1$ , leading to significant optical depth  $OD = 4\beta M$ . Our diagrammatic approach takes advantage of the weak coupling and uses  $\beta$  as an expansion parameter, which enables us to analytically compute leading-order contributions to the three-photon-correlated component of the wavefunction and the connected third-order correlation function  $g_c^{(3)}$ . We confirm the presence of light with significant non-Gaussian correlations ( $|g_c^{(3)}| > 0.1$ ) for weakly driven atomic ensembles of moderate optical depth  $OD \sim 2$ .

**Model.**—The model for our system is depicted in Fig. 1, where  $M$  atoms are unidirectionally coupled to a propagating channel in a waveguide. Here we have illustrated

the example of a nanofibre geometry where atoms are trapped near the fibre and interact via its evanescent field. Each atom couples to the propagating channel at rate  $\Gamma = \beta\Gamma_{\text{tot}}$  and to its individual loss channel at rate  $\gamma = (1 - \beta)\Gamma_{\text{tot}}$ , where  $\beta$  quantifies the coupling efficiency and  $\Gamma_{\text{tot}}$  is the overall atomic decay rate. The emitters are driven by a coherent on-resonance driving field from one end of the waveguide. The emitter spacing exceeds one resonant wavelength of the two-level atoms which ensures negligible collective emission outside the waveguide. Typical experimental values for atomic ensembles coupled to nanofibres yield  $\beta \sim 0.01$  [3]. Despite the small individual coupling strength, the OD of the entire atomic array becomes significant  $\text{OD} = \mathcal{O}(1)$ , where  $\mathcal{O}(\cdot)$  indicates big-O notation. This enables the collective nonlinear effects and strong dissipation to substantially modulate photon transport properties, which, as we show, results in strongly correlated photons and non-Gaussian output states of light.

The local scattering event at the  $m$ th atom is described by a one-dimensional two-channel model, where each atom interacts with the waveguide and a loss channel. The Hamiltonian is (with  $\hbar = c = 1$ ),

$$\hat{H}_m = \int_{-\infty}^{\infty} dx \left\{ \hat{a}^\dagger(x)(-i\partial_x)\hat{a}(x) + \hat{b}_m^\dagger(x)(-i\partial_x)\hat{b}_m(x) + \delta(x) \left[ \hat{\sigma}_m^+(\sqrt{\Gamma}\hat{a}(x) + \sqrt{\gamma}\hat{b}_m(x)) + h.c. \right] \right\}, \quad (1)$$

where  $\hat{a}^\dagger(x)$  and  $\hat{b}_m^\dagger(x)$  create photons in the propagating and  $m$ th atom's loss channels respectively, while  $\hat{\sigma}_m^\pm$  are Pauli operators for the  $m$ th two-level emitter.

By applying the following Weyl transformation,  $\hat{a}_m^{(e)}(x) = \sqrt{\beta}\hat{a}(x) + \sqrt{1-\beta}\hat{b}_m(x)$ ,  $\hat{a}_m^{(o)}(x) = \sqrt{1-\beta}\hat{a}(x) - \sqrt{\beta}\hat{b}_m(x)$ , (1) splits into two decoupled even and odd channels. The odd channel Hamiltonian  $\hat{H}_m^{(o)}$  describes non-interacting transport. All the information about atom-photon and photon-photon interactions at the  $m$ th atom is encoded in the even channel Hamiltonian  $\hat{H}_m^{(e)}$  with interaction strength  $\Gamma_{\text{tot}}$ ,

$$\begin{aligned} \hat{H}_m &= \hat{H}_m^{(e)} + \hat{H}_m^{(o)}, \quad \hat{H}_m^{(o)} = \int_{-\infty}^{\infty} dx \hat{a}_m^{\dagger(o)}(x)(-i\partial_x)\hat{a}_m^{(o)}(x) \\ \hat{H}_m^{(e)} &= \int_{-\infty}^{\infty} dx \left\{ \hat{a}_m^{\dagger(e)}(x)(-i\partial_x)\hat{a}_m^{(e)}(x) + \delta(x)\sqrt{\Gamma_{\text{tot}}} \left[ \hat{\sigma}_m^+ \hat{a}_m^{(e)}(x) + h.c. \right] \right\}. \end{aligned} \quad (2)$$

The  $n$ -photon scattering in the even subspace can be fully described by the  $S$ -matrix derived from Bethe's Ansatz [25, 26]. The full  $S$ -matrix element encodes all the information of free propagation of photons, photon-atom and photon-photon interactions. We refer to free

propagation of photons and individual elastic photon-atom scattering as *disconnected processes* because they factorize into independent terms in the  $S$ -matrix. The *connected part* of  $S$ -matrix is defined by subtracting all the products of the disconnected processes from the full  $S$ -matrix, enabling us to extract the genuine effects of  $n$ -body photon-photon interactions [27]. The expression of the full and connected two- and three-photon  $S$ -matrix is given in the accompanying work [28].

The local scattering event at the  $m$ th atom can be calculated by the following steps: (1) transform the incoming state from the propagating channel into even/odd channel picture (2) multiply the term with  $n$  even photons by the  $n$ -photon  $S$ -matrix (3) transform back to propagating/loss channel picture. When the photon remains in the waveguide, elastic single-photon scattering reduces to multiplication by the  $k$ -space transmission coefficient  $t_k = 1 - i\beta\Gamma_{\text{tot}}/(k + i\Gamma_{\text{tot}}/2)$ , while two- and three-photon interaction events are captured by the multiplications of their respective connected scattering matrices  $\beta^2 \hat{S}_{p_1 p_2, k_1 k_2}^C$  and  $\beta^3 \hat{S}_{p_1 p_2 p_3, k_1 k_2 k_3}^C$ . When a photon is lost by elastic scattering out of the waveguide, the incoming state is multiplied by a reflection coefficient  $r_k = -\sqrt{\beta(1-\beta)}i\Gamma_{\text{tot}}/(k + i\Gamma_{\text{tot}}/2)$ . Alternatively, if loss occurs immediately after a two- or three-photon interaction, the incoming state is multiplied by  $\beta^{3/2}\sqrt{(1-\beta)}\hat{S}_{p_1 p_2, k_1 k_2}^C$  or  $\beta^{5/2}\sqrt{(1-\beta)}\hat{S}_{p_1 p_2 p_3, k_1 k_2 k_3}^C$  respectively.

Expressing the scattering in terms of the connected part of the  $S$ -matrix clarifies the way in which genuine photon-photon interactions scale with the various powers of coupling strength  $\beta$ . Since  $\beta \ll 1$ , this scaling behavior motivates us to perturbatively treat the effect of photon-photon interactions in terms of the order in  $\beta$ . If a three-photon transport process has no photon-photon interaction, the outgoing state is simply the incoming state of the array multiplied by  $t_0^{3M}$ . Transport processes generating three-photon correlations are the main interest of this work. In Fig. 2, we sketch the interaction processes where three-photon trajectories are connected by interaction lines. These diagrams are drawn according to the following rules: (1) Each horizontal line indicates the trajectory of each photon being transported through the array from the left to the right. The individual elastic atom-photon scatterings are not explicitly indicated on the line. (2) Each black circular dot on the photon trajectory represents an atomic site where the photon interacts with other photons. The dots on the same column corresponds to the same atomic site. (3) A  $n$ -photon interaction is represented by a wavy line connecting  $n$  dots. We note that black dots can be any atom in the array, therefore each diagram in Fig. 2 represents all possible transport processes with the interactions happening on different atomic sites. For example, Fig. 2(a) shows three photons interacting via a single atom. This can occur at any atom within the ensemble and therefore

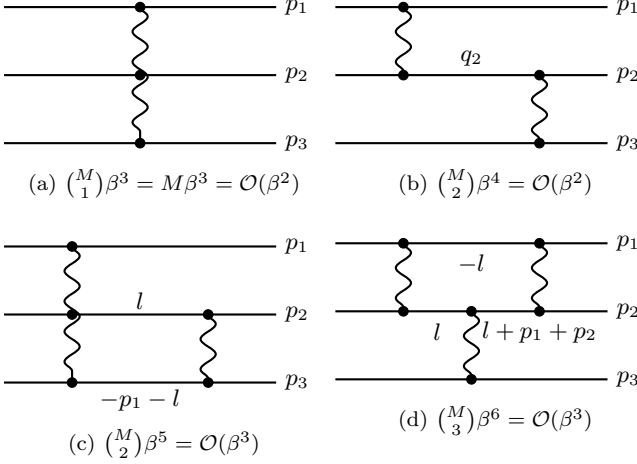


FIG. 2. Diagrammatic representation of the terms in  $T^{(1)}$ , which is the major contribution to the non-Gaussianity of outgoing light. The diagram including one three-photon interaction is called 3-vertex diagram, and the diagram including two two-photon interactions is called 4-vertex diagram. The momentum of the photons after the interaction is labeled above the horizontal line. The line piece without momentum labels mean the photon is on resonance with the atom. The order estimates below each diagram show their respective scaling behavior in the large optical depth regime.

has a combinatorial factor of  $M$ . Photon-photon interactions at the start of the ensemble are more likely as each elastic scattering before the photon-photon interaction multiplies the photon wavefunction by  $t_0$ , exponentially decreasing its amplitude along the array.

Based on the transport processes sketched in Fig. 2, the scattering matrices for the 3- and 4-vertex diagrams can be written as follows. For resonant input photons, the 3-vertex diagram (Fig. 2(a)) is expressed as

$$\hat{T}^{3v} = \sum_{j=0}^{M-1} (t_{p_1} t_{p_2} t_{p_3})^{M-j-1} \beta^3 \hat{S}_{p_1 p_2 p_3, 000}^C t_0^{3j}, \quad (3)$$

where each term describes  $j$  individual single-photon scatterings, followed by a three-photon interaction at site  $j+1$ , and the remaining  $M-j-1$  individual single-photon scatterings. For the 4-vertex diagram (Fig. 2(b)),

$$\begin{aligned} \hat{T}^{4v} = & \sum_{j=0}^{M-2} \sum_{m=0}^{M-j-2} t_{p_1}^{M-j-1} (t_{p_2} t_{p_3})^{M-j-m-2} \beta^2 \hat{S}_{p_2 p_3, q_2 0}^C \\ & \times t_{q_2}^m \beta^2 \hat{S}_{p_1 q_2, 00}^C t_0^{3j+m+1}, \end{aligned} \quad (4)$$

where after  $j$  individual single-photon scatterings, the first two-photon interaction occurs at site  $j+1$ ; the middle photon with momentum  $q_2$  then undergoes  $m$  additional individual single-photon scatterings before the second two-photon interaction at site  $j+m+2$ , followed by the remaining  $M-j-m-2$  individual single-photon

scatterings. Due to the bosonic symmetry, there are six 4-vertex diagrams corresponding to different permutations of the outgoing momenta  $p_1, p_2, p_3$  at the right end of the diagram. To estimate the order of the amplitude of each diagram for perturbative expansion, we need to consider (1) the weight of the coupling constant  $\beta$ , and (2) the combinatorics of the process due to interactions potentially occurring at any atom in the ensemble. For (1), we follow how photon-creation operators transform under Weyl transformation for nonlinear interactions. Each transmitted photon picks up a factor  $\sqrt{\beta}$  when moving from the propagating to the even channel and another  $\sqrt{\beta}$  when transforming back to the propagating channel, giving an overall factor  $\beta$ . This means the wavefunction amplitude of a single two-photon interaction scales as  $\beta^2$ , while a single three-photon interaction scales as  $\beta^3$ . For a lost photon, the second factor becomes  $\sqrt{1-\beta}$ , so the vertex contributes  $\sqrt{\beta(1-\beta)} \approx \sqrt{\beta}$ . For (2), the combinatorics of a diagram with  $n$  photon-photon interactions is  $\binom{M}{n}$ . For larger OD  $\beta M = \mathcal{O}(1)$ , the magnitude is estimated by multiplying  $\beta$  and the combinatorial factor. For example, the order of Fig. 2b is  $\binom{M}{2} \beta^4 \approx M^2 \beta^4 = \mathcal{O}(\beta^2)$ . For the order estimation in small or intermediate OD, because the power of  $\beta$  is fixed for each diagram, its magnitude grows monotonically with  $M$ , therefore the leading diagrams at small or intermediate OD are a subset of those at large OD. Hence, perturbative results derived for the large-OD regime remain valid, and even gain accuracy, when applied to lower-OD systems.

From the Eq. 3 and 4, we see that at large OD,  $\hat{T}^{3v}$  and  $\hat{T}^{4v}$  are both at  $\mathcal{O}(\beta^2)$ , which is the leading-order contribution among all possible three-photon-connected diagrams. The subleading order  $\mathcal{O}(\beta^3)$  three-photon connected diagrams includes two types of diagrams: (1) the diagrams with one three-photon interaction and one two-photon interaction, and (2) the diagrams with three two-photon interactions. One representative of each type is shown in Figs. 2c and 2d. These diagram are negligible at  $\beta \approx 1\%$ , but are significant at large OD with  $\beta \approx 5\%$ . As the diagrams feature a loop structure, we refer to these as loop-order diagrams and their explicit calculation is presented in our accompanying work [28].

So far we only considered the incoming state of the array as three-photon Fock state. For an on-resonance coherent state input  $|\alpha\rangle = e^{-\alpha^2/2} \sum_{n=0}^{\infty} \frac{P_{\text{in}}^{n/2}}{n!} \int_{-L/2}^{L/2} dx_j \hat{a}^\dagger(x_j) |0\rangle$ , where  $L$  is the quantization length, and  $P_{\text{in}} = |\alpha|^2/L$  is the input power density per unit length. In the thermodynamic limit  $L, |\alpha|^2 \rightarrow \infty$  with fixed  $P_{\text{in}}$ . To apply our scattering theoretic approach for coherent input, we employ the following assumption: In the  $n$ -photon component of the coherent input, we assume that exactly  $k$  photons participate in the interaction processes represented by a given  $k$ -photon diagram (with  $k = 3$

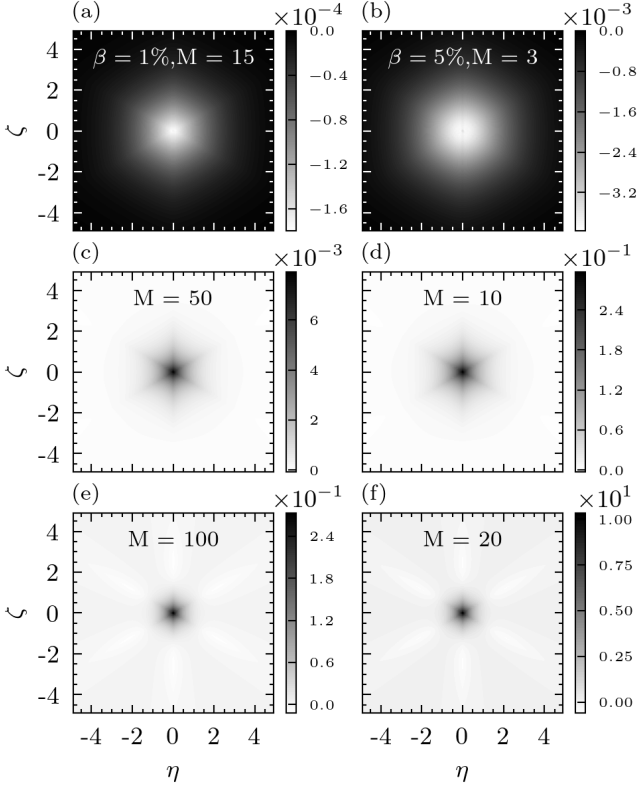


FIG. 3. Connected third-order correlation function with various OD  $g_c^{(3)}(R, \eta, \zeta)$  in Jacobi coordinates, with center of mass  $R = 0$ . The six-fold symmetry reflects three symmetry axes corresponding to two-photon coincidences.  $g_c^{(3)}$  is computed at tree-level diagram for  $\beta = 1\%$  while the loop order correction is added for  $\beta = 5\%$

presented in Fig. 2), while the remaining  $n - k$  photons scatter independently (being transmitted or lost one by one). Consequently, the amplitude for that  $n$ -photon sector factorizes into the  $k$ -photon diagram amplitude multiplied by the single-photon amplitudes for the other  $n - k$  photons; the full output is obtained by summing this factorized contribution over  $n$  and every allowed configuration of the extra  $n - k$  photons.

*Connected third-order correlation function.*—Having identified the leading-order contributions to connected three-photon scattering, we now translate this into an experimentally accessible quantity that indicates the non-Gaussianity of the outgoing light. The connected third-order correlation function is defined as

$$g_c^{(3)}(x_1, x_2, x_3) = 2 + g^{(3)}(x_1, x_2, x_3) - \sum_{i < j} g^{(2)}(x_i, x_j), \quad (5)$$

where  $g^{(2)}(x_1, x_2)$  and  $g^{(3)}(x_1, x_2, x_3)$  are the normalized second- and third-order correlation functions, respectively. For non-vanishing power,  $g_c^{(3)}(x_1, x_2, x_3)$  vanishes when either one photon is far away from the other two, or when the state of the light is

Gaussian [8, 29, 30]. In the weak driving condition  $\mathcal{O}(P_{\text{in}}/\Gamma_{\text{tot}}) = \mathcal{O}(\beta)$  [31],  $g^{(n)}(x_1, \dots, x_n) = \langle : \Pi_{j=1}^n \hat{a}^\dagger(x_j) \hat{a}(x_j) : \rangle / \Pi_{k=1}^n \langle \hat{a}^\dagger(x_k) \hat{a}(x_k) \rangle$  for  $n = 2, 3$  can be approximated as:

$$g^{(3)}(x_1, x_2, x_3) \approx |\psi_3(x_1, x_2, x_3)|^2 / t_0^{6M}, \\ g^{(2)}(x_1, x_2) \approx |\psi_2(x_1, x_2)|^2 / t_0^{4M}, \quad (6)$$

where  $\psi_2(x_1, x_2) = t_0^{2M} + \phi_2(x_1, x_2)$  with  $\phi_2(x_i, x_j)$  is the entangled wavefunction generated by all possible two-photon interactions. The output power  $\langle \hat{a}^\dagger(x) \hat{a}(x) \rangle \approx P_{\text{in}} t_0^{2M}$ ,  $\psi_3(x_1, x_2, x_3) = t_0^{3M} + t_0^M \sum_{1 \leq i < j \leq 3} \phi_2(x_i, x_j) + \phi_3(x_1, x_2, x_3)$ , where  $\phi_3$  encodes the correlation induced by leading- and subleading-order three-photon interactions depicted in Fig. 2. We evaluate  $\phi_2$  and  $\phi_3$  analytically, but for brevity here, their expressions are given in [28].

In Fig. 3 we plot the connected third-order correlation  $g_c^{(3)}(x_1, x_2, x_3)$  using the approximation (6) for an atomic ensemble with  $\beta = 1\%$  and  $5\%$ . The value  $\beta = 1\%$  represents the approximate value from past experiments [3, 6, 21], while  $\beta = 5\%$  is what could be obtained if the atoms are trapped more closely to the fibre and/or if the light-matter coupling is enhanced, for example, with slow light using fibre gratings. The result of  $g_c^{(3)}(x_1, x_2, x_3)$  is shown in Jacobi coordinates  $R = \frac{x_1 + x_2 + x_3}{\sqrt{3}}$ ,  $\eta = \frac{x_1 - x_2}{\sqrt{2}}$ ,  $\zeta = \sqrt{\frac{2}{3}} \left( \frac{x_1 + x_2}{2} - x_3 \right)$  with  $R = 0$  fixed by translational invariance. In the  $\eta$ - $\zeta$  plane,  $g_c^{(3)}$  exhibits an apparent six-fold symmetry: the underlying three-fold bosonic permutation symmetry is doubled because  $g_c^{(3)}$  does not distinguish whether a photon pair arrives before or after the lone photon. As the optical depth increases,  $g_c^{(3)}$  evolves from being everywhere negative, through a regime of uniform positivity, to a characteristic pattern with a bright central peak surrounded by six negative “outer legs.” Under approximation (6),  $g_c^{(3)}(x_1, x_2, x_3) = 2\phi_3(x_1, x_2, x_3)/t_0^{3M} + 2[\phi_2(x_2, x_1)\phi_2(x_1, x_3) + \phi_2(x_1, x_2)\phi_2(x_2, x_3) + \phi_2(x_1, x_3)\phi_2(x_3, x_2)]/t_0^{4M} + \mathcal{O}(\beta^3)$ . The low-OD behaviour is dominated by the amplitude of the 3-vertex diagram transport in  $\phi_3$  because it has the lowest power in  $\beta$ . This amplitude carries a negative sign in position space. As OD increases, the amplitude of the 4-vertex diagram contribution to  $\phi_3$  (with a positive sign) becomes significant. Meanwhile, the second term—being the product of two negative  $\phi_2$  amplitudes—adds a net positive contribution. The competition between various transport mechanism at different OD explain the observed sign reversal and the emergence of the six-lobed pattern at high optical depth.

When the number of the atoms is small  $M \leq 11$ ,  $g_c^{(3)}$  can be numerically calculated using the quantum regression theorem (QRT) and the cascaded master equation. The comparison between  $g_c^{(3)}$  obtained by our theory and simulation is given in Fig. 6. To benchmark the

accuracy of our perturbative calculation, we computed  $g_c^{(3)}(x_1, x_2, 0)$  on a  $50 \times 50$  grid ( $x_1, x_2 \in [0, 5/\Gamma_{\text{tot}}]$ ) using both our diagrammatic analytic calculation and QRT, yielding matrices  $\mathcal{M}$  and  $\mathcal{M}'$ , respectively. We calculate the relative error between theory and QRT using  $\epsilon = \|\mathcal{M} - \mathcal{M}'\|_F / \|\mathcal{M}\|_F$ , where  $\|\cdot\|_F$  is the Frobenius norm. For an array with  $\beta = 5\%$ ,  $\epsilon < 2.0\%$  and  $\epsilon < 6.2\%$  for drive powers  $P_{\text{in}} = 0.02\Gamma_{\text{tot}}$  and  $P_{\text{in}} = 0.06\Gamma_{\text{tot}}$  respectively. These results confirm the quantitative accuracy of our loop-level perturbative method at low OD ( $\text{OD} \leq 0.4$ ). We also see from Fig. 6 that even though the value of  $g_c^{(3)}$  diminishes at higher power  $P_{\text{in}} \geq 0.4\Gamma_{\text{tot}}$ , the simulations still qualitatively agree with the theory at  $\text{OD} > 1$ . This is because: for the approximation (6) under the weak-drive condition, we only considered three-photon diagrams for  $g^{(3)}$  and two-photon diagrams for  $g^{(2)}$ . When the drive power is further increased to  $P_{\text{in}}/\Gamma_{\text{tot}} = \mathcal{O}(1)$ ,  $P_{\text{in}}/\Gamma_{\text{tot}}$  is no longer a good expansion parameter, and thus the photon transport diagrams with more photons, such as Figs. 4-5, should be taken into consideration.

To observe correlated/anti-correlated photon triples,  $P_{\text{in}}$  and OD should be chosen such that  $|g_c^{(3)}|$  is sufficiently large and the count rate of triples should be in the detectable range. We estimate the experimental counting rate  $\mathcal{S}$  of arriving within the window time  $3/\Gamma_{\text{tot}}$  as

$$\mathcal{S} = \int_0^{3/\Gamma_{\text{tot}}} dt_1 dt_2 |G_c^{(3)}(t_1, t_2, 0)|. \quad (7)$$

Here,  $G_c^{(3)}(t_1, t_2, t_3) = g_c^{(3)} \prod_{j=1}^3 \langle \hat{a}^\dagger(t_j) \hat{a}(t_j) \rangle$ . We consider parameters  $\Gamma_{\text{tot}} = 2\pi \times 5$  MHz and fixed driving strength  $P_{\text{in}} = 0.06\Gamma_{\text{tot}}$ . For an OD range with detectable three-photon correlations such that  $|g_c^{(3)}| \geq 0.1$ , our estimation shows that the correlated-triple-photon count rate is 5 Hz and 2 Hz for  $\beta = 5\%$ ,  $M = 8$  and  $\beta = 1\%$ ,  $M = 85$ , respectively. For larger powers,  $\mathcal{S} \propto P_{\text{in}}^3$ , and thus  $\mathcal{S}$  increases rapidly. This comes only at the expense of a slightly reduced  $|g_c^{(3)}|$  as shown in the simulations Fig. 6. This is because most correction diagrams, shown in Figs. 4-5, decay exponentially with OD. Therefore, experiments can adjust driving strengths to balance count rates and  $|g_c^{(3)}|$ .

*Conclusion.*—We have developed a diagrammatic scattering theory to calculate three-photon transport through weakly coupled atomic ensembles. Our formalism provides analytic expression of the leading-order processes that contribute to non-separable three-photon correlations. We have used our new approach to predict the presence of non-Gaussian correlations in the transmitted field of coherently driven atomic ensembles. We anticipate our results will pave the way for experimental demonstration of sources of non-Gaussian photon states using atoms coupled to nanofibres.

*Acknowledgements.*—S.M. acknowledges support from

the Australian Research Council (ARC) via the Future Fellowship, ‘Emergent many-body phenomena in engineered quantum optical systems’, project no. FT200100844. Y.W. acknowledges the financial support from Sydney Quantum Academy, Sydney, NSW, Australia.

---

\* ywan8652@uni.sydney.edu.au

† sahand.mahmoodian@sydney.edu.au

- [1] S. Mahmoodian, M. Čepulkovskis, S. Das, P. Lodahl, K. Hammerer, and A. S. Sørensen, Strongly correlated photon transport in waveguide quantum electrodynamics with weakly coupled emitters, *Phys. Rev. Lett.* **121**, 143601 (2018).
- [2] A. S. Sheremet, M. I. Petrov, I. V. Iorsh, A. V. Poshakinskiy, and A. N. Poddubny, Waveguide quantum electrodynamics: Collective radiance and photon-photon correlations, *Rev. Mod. Phys.* **95**, 015002 (2023).
- [3] A. S. Prasad, J. Hinney, S. Mahmoodian, K. Hammerer, S. Rind, P. Schneeweiss, A. S. Sørensen, J. Volz, and A. Rauschenbeutel, Correlating photons using the collective nonlinear response of atoms weakly coupled to an optical mode, *Nat. Photonics* **14**, 719 (2020).
- [4] M. Cordier, M. Schemmer, P. Schneeweiss, J. Volz, and A. Rauschenbeutel, Tailoring photon statistics with an atom-based two-photon interferometer, *Phys. Rev. Lett.* **131**, 183601 (2023).
- [5] G. Ferioli, I. Ferrier-Barbut, and A. Browaeys, Emergence of second-order coherence in the superradiant emission from a free-space atomic ensemble, *Phys. Rev. Lett.* **134**, 153602 (2025).
- [6] J. Hinney, A. S. Prasad, S. Mahmoodian, K. Hammerer, A. Rauschenbeutel, P. Schneeweiss, J. Volz, and M. Schemmer, Unraveling two-photon entanglement via the squeezing spectrum of light traveling through nanofiber-coupled atoms, *Phys. Rev. Lett.* **127**, 123602 (2021).
- [7] Z. H. Lu, S. Bali, and J. E. Thomas, Observation of squeezing in the phase-dependent fluorescence spectra of two-level atoms, *Phys. Rev. Lett.* **81**, 3635 (1998).
- [8] N. Stiesdal, J. Kumlin, K. Kleinbeck, P. Lunt, C. Braun, A. Paris-Mandoki, C. Tresp, H. P. Büchler, and S. Hofferberth, Observation of three-body correlations for photons coupled to a rydberg superatom, *Phys. Rev. Lett.* **121**, 103601 (2018).
- [9] Q.-Y. Liang, A. V. Venkatramani, S. H. Cantu, T. L. Nicholson, M. J. Gullans, A. V. Gorshkov, J. D. Thompson, C. Chin, M. D. Lukin, and V. Vuletić, Observation of three-photon bound states in a quantum nonlinear medium, *Science* **359**, 783 (2018).
- [10] D. P. Ornelas-Huerta, P. Bienias, A. N. Craddock, M. J. Gullans, A. J. Hachtel, M. Kalinowski, M. E. Lyon, A. V. Gorshkov, S. L. Rolston, and J. V. Porto, Tunable three-body loss in a nonlinear rydberg medium, *Phys. Rev. Lett.* **126**, 173401 (2021).
- [11] N. Tomm, S. Mahmoodian, N. O. Antoniadis, R. Schott, S. R. Valentin, A. D. Wieck, A. Ludwig, A. Javadi, and R. J. Warburton, Photon bound state dynamics from a single artificial atom, *Nature Physics* **19**, 857 (2023).
- [12] B. C. Das, A. Harkavi, A. Prakash, A. Nakav,

- L. Drori, and O. Firstenberg, Quantum nonlinear optics with counter-propagating photons, arXiv preprint arXiv:2506.01124 (2025).
- [13] G. Ferioli, S. Pancaldi, A. Glicenstein, D. Clément, A. Browaeys, and I. Ferrier-Barbut, Non-gaussian correlations in the steady state of driven-dissipative clouds of two-level atoms, *Phys. Rev. Lett.* **132**, 133601 (2024).
  - [14] C. Weedbrook, S. Pirandola, R. García-Patrón, N. J. Cerf, T. C. Ralph, J. H. Shapiro, and S. Lloyd, Gaussian quantum information, *Rev. Mod. Phys.* **84**, 621 (2012).
  - [15] S. L. McCall and E. L. Hahn, Self-induced transparency, *Phys. Rev.* **183**, 457 (1969).
  - [16] K. Hammerer, A. S. Sørensen, and E. S. Polzik, Quantum interface between light and atomic ensembles, *Rev. Mod. Phys.* **82**, 1041 (2010).
  - [17] D. Gonçalves, L. Bombieri, G. Ferioli, S. Pancaldi, I. Ferrier-Barbut, A. Browaeys, E. Shahmoon, and D. Chang, Driven-dissipative phase separation in free-space atomic ensembles, *PRX Quantum* **6**, 020303 (2025).
  - [18] K. J. Kusmierek, M. Schemmer, S. Mahmoodian, and K. Hammerer, Emergence of unidirectionality and phase separation in optically dense emitter ensembles, arXiv preprint arXiv:2412.14930 (2024).
  - [19] C. W. Gardiner, Driving a quantum system with the output field from another driven quantum system, *Phys. Rev. Lett.* **70**, 2269 (1993).
  - [20] H. J. Carmichael, Quantum trajectory theory for cascaded open systems, *Phys. Rev. Lett.* **70**, 2273 (1993).
  - [21] K. J. Kusmierek, S. Mahmoodian, M. Cordier, J. Hiney, A. Rauschenbeutel, M. Schemmer, P. Schneeweiss, J. Volz, and K. Hammerer, Higher-order mean-field theory of chiral waveguide qed, *SciPost Phys. Core* **6**, 041 (2023).
  - [22] D. Plankensteiner, C. Hotter, and H. Ritsch, Quantum-cumulants.jl: A julia framework for generalized mean-field equations in open quantum systems, *Quantum* **6**, 617 (2022).
  - [23] M. T. Manzoni, D. E. Chang, and J. S. Douglas, Simulating quantum light propagation through atomic ensembles using matrix product states, *Nature communications* **8**, 1743 (2017).
  - [24] S. Mahmoodian, G. Calajó, D. E. Chang, K. Hammerer, and A. S. Sørensen, Dynamics of many-body photon bound states in chiral waveguide qed, *Phys. Rev. X* **10**, 031011 (2020).
  - [25] V. I. Yudson, Dynamics of integrable quantum systems, *Zh. Eksp. Teor. Fiz.* **88**, 1757 (1985).
  - [26] V. Rupasov and V. Yudson, Exact dicke superradiance theory: Bethe wavefunctions in the discrete atom model, *Zh. Eksp. Teor. Fiz* **86**, 819 (1984).
  - [27] S. Weinberg, *The Quantum Theory of Fields: Volume I* (Cambridge University Press, 1995).
  - [28] Y. Wang, N. Demazure, and S. Mahmoodian, Theory of three-photon transport through a weakly coupled atomic ensemble (2025), arXiv:2507.03428 [quant-ph].
  - [29] M.-A. Lemonde, N. Didier, and A. A. Clerk, Antibunching and unconventional photon blockade with gaussian squeezed states, *Phys. Rev. A* **90**, 063824 (2014).
  - [30] K. Jachymski, P. Bienias, and H. P. Büchler, Three-body interaction of rydberg slow-light polaritons, *Phys. Rev. Lett.* **117**, 053601 (2016).
  - [31] Stricly, we require  $\mathcal{O}(P_{\text{in}}/\Gamma_{\text{tot}}) = \mathcal{O}(\beta^2)$ , but it is shown in the accompanying work [28] that this condition can be

loosened to be  $\mathcal{O}(P_{\text{in}}/\Gamma_{\text{tot}}) = \mathcal{O}(\beta)$ .

## End Matter

### The Diagrams for the non-Perturbative Drive Regime

In the weak-driving regime, where  $\mathcal{O}(P_{\text{in}}/\Gamma_{\text{tot}}) = \mathcal{O}(\beta)$ , the order estimation combined with the approximation (6) indicates that it suffices to consider single-, two-, and three-photon diagrams for evaluating the correlators  $\langle : \prod_{j=1}^n \hat{a}^\dagger(x_j) \hat{a}(x_j) : \rangle$  with  $n = 1, 2, 3$ , respectively, in order to obtain  $g_c^{(3)}(x_1, x_2, x_3)$ . When the drive power increases to  $P_{\text{in}}/\Gamma_{\text{tot}} = \mathcal{O}(1)$ , the diagrams with additional photons must be included in each  $\langle : \prod_{j=1}^n \hat{a}^\dagger(x_j) \hat{a}(x_j) : \rangle$  to obtain an accurate perturbative result. This, however, becomes formidable due to the rapid growth in combinatorial complexity of diagrams.

Numerical simulations in Fig. 6 reveal that  $g_c^{(3)}$  exhibits markedly different temporal patterns under weak and strong driving at small OD, but the two regimes appear similar at large OD. This suggests that the contribution from the temporally dependent part of additional-photon diagrams may decay rapidly with OD. To illustrate this, we list below several representative terms from the diagrams with more photons and show their scaling with various powers of  $t_0^M$ . In the figures on the left, the coordinate  $x_j$  attached to the end of a photon-transport line denotes the outgoing photons contracted with the  $\hat{a}(x_j)$  or  $\hat{a}^\dagger(x_j)$  operator in the definition of the correlators. The cross attached at the end of the photon line indicates that the photon is lost at some atom in the array. These diagrams form part of the total sum represented by the figures on the right.

First, we examine the additional diagrams contributing to  $\langle \hat{a}^\dagger(x) \hat{a}(x) \rangle$ . Owing to the translational invariance of the steady state, these diagrams—like the output power itself—are independent of  $x$ . The representative term shown on the left in Fig. 4a scales as  $t_0^{4M}$ . In many cases, the scaling with the exponential decay factor  $t_0^M$  can be inferred without performing the full, laborious diagrammatic evaluation of the expectation value. Instead, one can exploit the connectedness of the diagrams and momentum conservation in photon-photon interactions. For example, in Fig. 4a, the bra diagram contributes a factor  $t_0^{2M}$ . When evaluating the expectation value, the bottom photons in the bra and ket contract, enforcing the same outgoing zero momentum. Momentum conservation in the photon-photon interaction within the ket then requires the top photon in the ket to also have zero momentum. Since both photons have zero momentum before and after the interaction, the amplitude is  $\sim t_0^{2M}$ . From an explicit calculation for Fig. 4b (not shown here) we have seen that it does not exhibit explicit  $t_0^M$  scaling, implying that its contribution to  $g_c^{(3)}$  persists even as OD increases. However, because it enters  $\langle \hat{a}^\dagger(x) \hat{a}(x) \rangle$  in the denominator of  $g^{(3)}$  and  $g^{(2)}$  as a constant, it rescales the overall magnitude of the correlation functions with increasing  $P_{\text{in}}$ , without altering their temporal dependence.

$$\begin{aligned} \left\langle \text{---}x \middle| \text{---}x \right\rangle &\subset \left\langle \text{---} \middle| \hat{a}^\dagger(x) \hat{a}(x) \middle| \text{---} \right\rangle & \left\langle \text{---}x \middle| \text{---}x \right\rangle &\subset \left\langle \text{---} \middle| \hat{a}^\dagger(x) \hat{a}(x) \middle| \text{---} \right\rangle \\ \text{(a) } \mathcal{O}(\beta) & & \text{(b) } \mathcal{O}(\beta^2) \end{aligned}$$

FIG. 4. The representative additional term to the output power  $\langle \hat{a}^\dagger(x) \hat{a}(x) \rangle$ .

The terms which depends on the coordinate  $x_1$  and  $x_2$  appears in the additional diagram for  $\langle \hat{a}^\dagger(x_1) \hat{a}^\dagger(x_2) \hat{a}(x_2) \hat{a}(x_1) \rangle$  and for  $\langle \hat{a}^\dagger(x_1) \hat{a}^\dagger(x_2) \hat{a}^\dagger(x_3) \hat{a}(x_3) \hat{a}(x_2) \hat{a}(x_1) \rangle$ . However, by following a similar analysis to that in the previous paragraph, we see that both the representative terms in Fig. 5a and 5b scale with  $t_0^{4M}$ . Meanwhile, both the representative terms in Fig. 5c and 5d scale with  $t_0^{6M}$ . One could enumerate all the other temporal dependent terms from other additional diagrams at  $\mathcal{O}(\beta^2)$  to see that they all decay at least as fast as  $t_0^{4M}$ . This rapid decay of the temporal dependent terms explains why  $g_c^{(3)}$  exhibits similar temporal patterns at large OD when the system is under weak and strong drives.

$$\begin{aligned}
& \left\langle \begin{array}{c} \text{---} x_1 \\ \text{---} x_2 \end{array} \middle| \begin{array}{c} x_1 \\ x_2 \end{array} \text{---} \right\rangle \subset \left\langle \begin{array}{c} \text{---} \\ \text{---} \end{array} \middle| : \prod_{j=1}^2 \hat{a}^\dagger(x_j) \hat{a}(x_j) : \begin{array}{c} \text{---} \\ \text{---} \end{array} \right\rangle \quad \left\langle \begin{array}{c} \text{---} \times x_1 \\ \text{---} \times x_2 \end{array} \middle| \begin{array}{c} x_1 \\ x_2 \end{array} \text{---} \right\rangle \subset \left\langle \begin{array}{c} \text{---} \times \\ \text{---} \times \end{array} \middle| : \prod_{j=1}^2 \hat{a}^\dagger(x_j) \hat{a}^\dagger(x_j) : \begin{array}{c} \text{---} \times \\ \text{---} \times \end{array} \right\rangle \\
& \quad \text{(a) } \mathcal{O}(\beta^2) \qquad \qquad \qquad \text{(b) } \mathcal{O}(\beta^2) \\
& \left\langle \begin{array}{c} \text{---} x_1 \\ \text{---} x_2 \\ \text{---} x_3 \end{array} \middle| \begin{array}{c} x_1 \\ x_2 \\ x_3 \end{array} \text{---} \right\rangle \subset \left\langle \begin{array}{c} \text{---} \\ \text{---} \\ \text{---} \end{array} \middle| : \prod_{j=1}^3 \hat{a}^\dagger(x_j) \hat{a}(x_j) : \begin{array}{c} \text{---} \\ \text{---} \\ \text{---} \end{array} \right\rangle \quad \left\langle \begin{array}{c} \text{---} \times x_1 \\ \text{---} \times x_2 \\ \text{---} \times x_3 \end{array} \middle| \begin{array}{c} x_1 \\ x_2 \\ x_3 \end{array} \text{---} \right\rangle \subset \left\langle \begin{array}{c} \text{---} \times \\ \text{---} \times \\ \text{---} \times \end{array} \middle| : \prod_{j=1}^3 \hat{a}^\dagger(x_j) \hat{a}^\dagger(x_j) : \begin{array}{c} \text{---} \times \\ \text{---} \times \\ \text{---} \times \end{array} \right\rangle \\
& \quad \text{(c) } \mathcal{O}(\beta^2) \qquad \qquad \qquad \text{(d) } \mathcal{O}(\beta^2)
\end{aligned}$$

FIG. 5. The representative additional term to  $\langle \hat{a}^\dagger(x_1) \hat{a}^\dagger(x_2) \hat{a}(x_2) \hat{a}(x_1) \rangle$  in (a) and (b). These representative terms are proportional to  $t_0^{4M}$ , in the diagrams with additional photons. The representative additional term to  $\langle \hat{a}^\dagger(x_1) \hat{a}^\dagger(x_2) \hat{a}^\dagger(x_3) \hat{a}(x_3) \hat{a}(x_2) \hat{a}(x_1) \rangle$  in (c) and (d). These terms are nothing but the additional term for  $\langle \hat{a}^\dagger(x_1) \hat{a}^\dagger(x_2) \hat{a}(x_2) \hat{a}(x_1) \rangle$  multiplied by  $P_{\text{in}} t_0^{2M}$  because of the appearance of one more pair of contracted independent scattering photons at the bottom.

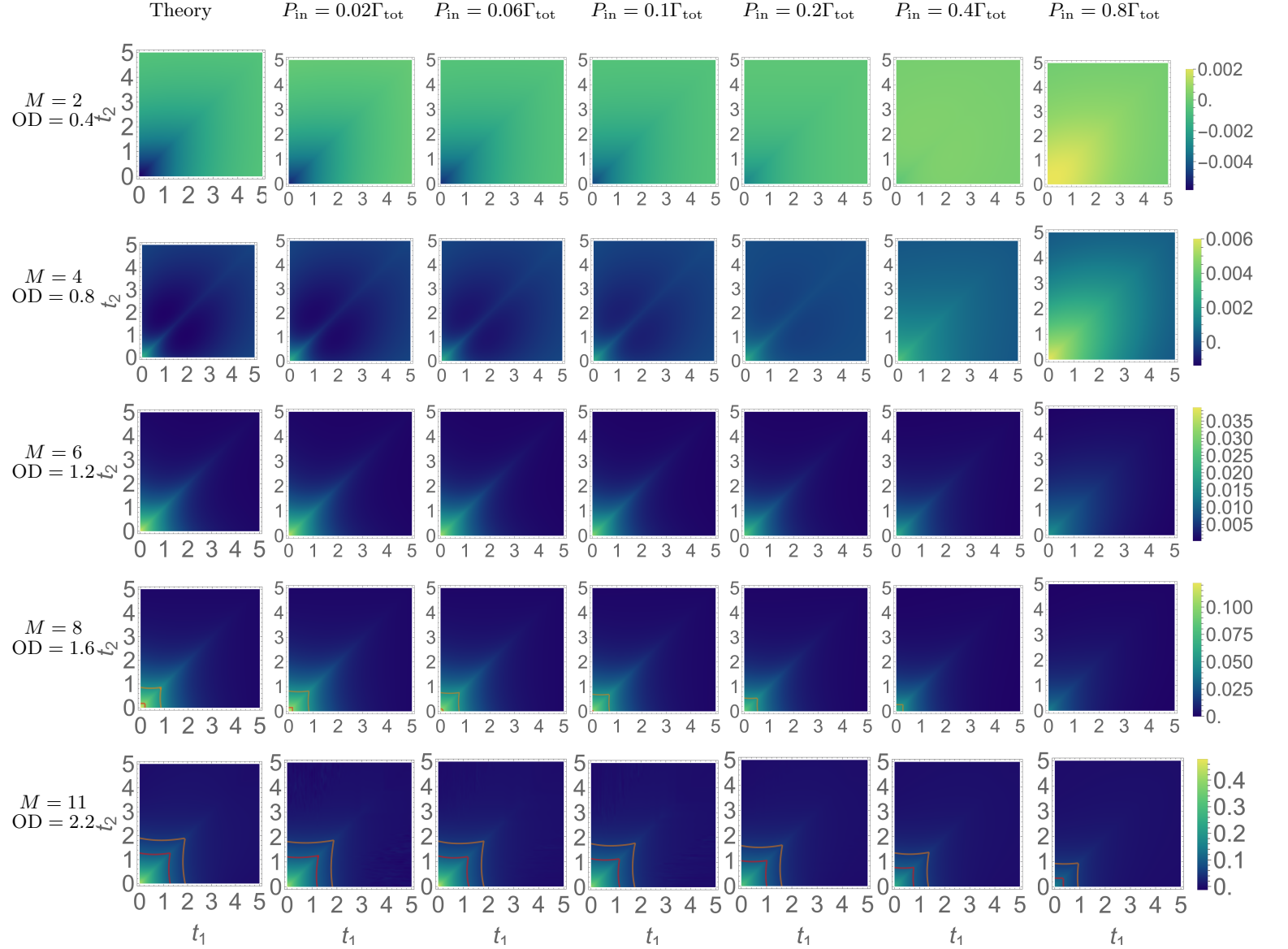


FIG. 6.  $g_c^{(3)}$  for the atomic ensemble-fibre system with coupling strength  $\beta = 5\%$  computed by our diagrammatic approach (the first column) and by simulation by using cascaded master equation with various driving power (the second to the last column). The orange and red contour line shows the region where  $|g_c^{(3)}|$  greater than 0.05 and 0.1, respectively.